



Magnetic Field and Plasma Density Observations of a Pressure Front by Voyager 1 during 2020 in the Very Local Interstellar Medium

L. F. Burlaga¹, W. S. Kurth², D. A. Gurnett², D. B. Berdichevsky^{3,4}, L. K. Jian⁵, N. F. Ness⁶, J. Park^{5,7}, and A. Szabo⁵

¹ Leonard F. Burlaga, Inc., Davidsonville, MD 21035, USA

² Department of Physics and Astronomy University of Iowa, Iowa City, IA 52242, USA

³ IFIR/CONICET-UNR, Esmeralda y 27 de Febrero, Rosario, Santa Fe, Argentina

⁴ TRIDENT—BERDICHEVSKY, DANIEL B. Partnership, Greenbelt, MD 20770, USA

⁵ Heliophysics Science Division, NASA/GSFC, Greenbelt, MD 20771, USA

⁶ Independent Scholar, Landenberg, PA 19350-9350, USA

⁷ University of Maryland, Baltimore County, Baltimore, MD 21250, USA

Received 2021 January 29; revised 2021 February 23; accepted 2021 March 1; published 2021 April 16

Abstract

Voyager 1 has been moving through the very local interstellar medium (VLISM) from the time that it crossed the heliopause on 2012/DOY 238 to 2020/DOY 292. Three notable objects in the magnetic field of the VLISM have been observed: two shocks and one pressure front. This paper reports the observation of a fourth object observed near 2020/DOY 147. There were no upstream electron plasma oscillations of the type often observed ahead of shocks, abrupt increases in energetic particles, or fluctuations in the 48 s increments of the magnetic field associated with this feature, suggesting that it was probably not a shock. This feature was associated with a relatively large increase in the magnetic field strength ($B_2/B_1 = 1.35$) and in the electron density determined by the Plasma Wave Science experiment ($N_2/N_1 = 1.36$) using a new method described in this paper. This feature appears to be a pressure front associated with a compressive wave in the VLISM. The two shocks and the two pressure fronts were associated with the four largest maxima observed in $B(t)$ between 2012/DOY 238 and 2020/DOY 292. Each feature was associated with a jump-ramp structure. The jump-ramp structures were separated by long relatively undisturbed quiet intervals.

Unified Astronomy Thesaurus concepts: [Interstellar magnetic fields \(845\)](#)

1. Introduction

The structure of the heliosphere, heliosheath, and heliopause and the interaction of the heliosphere with the interstellar medium was discussed by Holzer (1989), and reviewed by Zank (1999, 2015) and Zank (2015). The first indirect observation of a possible shock in the very local interstellar medium (VLISM) was made via remote radio measurements by Gurnett et al. (1993) using the Plasma Wave Science (PWS) instrument on Voyager 1 and was interpreted as being due to shocks propagating through a steeply increasing density in the interstellar medium immediately beyond the heliopause. This result motivated Whang & Burlaga (1995) to model the motion of a spherical shock driven by a global merged interaction region through the heliosphere, the termination shock, and the heliopause. Later, 3D numerical models of the interaction of a shock with the heliopause were published by Zank & Müller (2003), Washimi et al. (2011, 2017), Fermo et al. (2015), Kim et al. (2017), and others. Observations of solar wind and heliosheath structures that might lead to pressure pulses that are transmitted through the heliopause have been discussed, e.g., by Richardson et al. (2017) and Burlaga et al. (2016).

The Voyager 1 (V1) spacecraft crossed the heliopause into the VLISM at 122 au in 2012/DOY 210–238 near 35° latitude and 174° longitude (Burlaga et al. 2013b, 2014; Krimigis et al. 2013; Stone et al. 2013, and Gurnett et al. 2013).

A description of the magnetic field instruments on Voyager 1 and Voyager 2 is given by Behannon et al. (1977). A discussion of the processing of the data later in the mission, when the dual magnetometers were decoupled and used independently, is given by Berdichevsky (2009).

The original observations of the heliopause by V1 were surprising. The crossing of the heliopause occurred earlier than predicted by most models at that time (Karmesin et al. 1995; Wang & Belcher 1999; Zank & Müller 2003; McComas et al. 2010, 2013; Zank 2015; Pogorelov et al. 2017).

Voyager 1 observed multiple crossings of the heliopause, but there was no change in the direction of the magnetic field across the heliopause, contrary to all expectations. Fisk & Gloeckler (2014) and Gloeckler & Fisk (2014, 2016) proposed that V1 did not cross the heliopause. They predicted that V1 would observe a sector within a year or two, but no sector has been observed since V1 crossed the heliopause in 2012, thereby confirming the conclusion by Gurnett et al. (2013) that V1 had crossed the heliopause on or about 2012/DOY 210–238.

Shortly after crossing the heliopause, the magnetometer (MAG) on V1 recorded an abrupt increase in the magnetic field strength on 2012.92/330 to 340 (DOY 335), with a jump in the magnetic field $B_2/B_1 = 1.43$. This event was identified as a shock (sh1) (Burlaga et al. 2021), based on the observation that it was preceded by electron plasma oscillation events (Gurnett et al. 2013). The electron plasma oscillations showed that the electron density was $n_e = 0.05 \text{ cm}^{-3}$, indicating that the spacecraft was immersed in the dense interstellar medium. The last day during which electron plasma oscillations were



Original content from this work may be used under the terms of the [Creative Commons Attribution 4.0 licence](#). Any further distribution of this work must maintain attribution to the author(s) and the title of the work, journal citation and DOI.

observed was 2012/DOY 332, near the shock on 2012/DOY 335. Thus, it is highly probable that electron plasma oscillations were produced by electrons accelerated at a shock, in accordance with the theory and results of Fredricks et al. (1971) and as suggested in the model by Gurnett et al. (1993). This interpretation is generally accepted. However, the time interval during which the jump in B moved past Voyager 1 was 5.4 days, which is the order of 10^4 times that expected for a shock at 1 au. This result was not expected. Later, Mostafavi & Zank (2018a, 2018b) showed theoretically that a shock wave in the dense VLISM should be a collisional shock, and therefore the magnetic resistivity and viscosity would produce a shock that is much wider than the collisionless shocks observed in the interplanetary medium.

A second shock (sh2) was observed in the VLISM by V1 on 2014.6438 (2014/DOY 236) (Burlaga & Ness 2016). This shock was weaker than the previous one, with $B_1 = 0.48$ nT, $B_2 = 0.54$ nT, and the ratio $B_2/B_1 = 1.13$, which was smaller than that for the first shock. This shock, like the previous one, was laminar with no significant structure within it. The 2014 shock moved past V1 in 3.3 days. Thus, the two shocks observed in the VLISM, with jumps in $B = 1.4$ and 1.13, moved past V1 during intervals of 5.4 and 3.3 days, respectively. Both shocks were preceded by an interval containing electron plasma oscillations that were thought to be driven by low-energy, upstream electrons, which ended abruptly when the shock arrived (Gurnett et al. 2013, 2015, respectively). The presence of these electron plasma oscillations supports the interpretation of the abrupt jumps in B as shocks despite the large passage times, since it is known that electron plasma oscillations can be produced by a beam of electrons accelerated by a shock. These in situ observations of shocks in the VLISM beyond the heliopause confirm the hypothesis of Gurnett et al. (1993), based on the observations of a strong heliospheric 2–3 kHz radio emission event detected by Voyagers 1 and 2 that started in 1992 July, was generated at or near the heliopause by an interplanetary shock that originated during a period of intense solar activity in late May and early 1991 June. The latest results concerning plasma oscillations in the density ramp (Porgorelov et al. 2017) in the VLISM are discussed by Gurnett et al. (2021). In the ramps behind shocks sh1 and sh2, B decreased slowly and ended with small abrupt decreases in B on 2013/DOY 130 (2013.3534) and 2015/DOY 136 (2015.37) (Burlaga & Ness 2016), respectively.

A distinctly different feature, related to an increase in B moved past V1 in ~ 35 days during 2017 (Burlaga et al. 2019). The jump in B was 1.19, comparable to the jump in the second shock (1.13). However, this propagating structure was observed as an increase in B beginning on 2016/DOY ≈ 346 , rising to a local maximum much later, and declining nearly monotonically until day 720, measured from 2016.0. The event was not a shock wave, since the increase in B occurred during a ≈ 35 day interval (which is significantly larger than that predicted for collisional shocks by Mostafavi & Zank 2018a, 2018b) and it was not accompanied by intense impulsive plasma oscillations of the type normally driven by upstream electron beams associated with interstellar shocks. Burlaga et al. (2019) identified the event as a pressure front “pf1.” Since this was associated with a compressive wave that was propagating through the VLISM, presumably as a fast

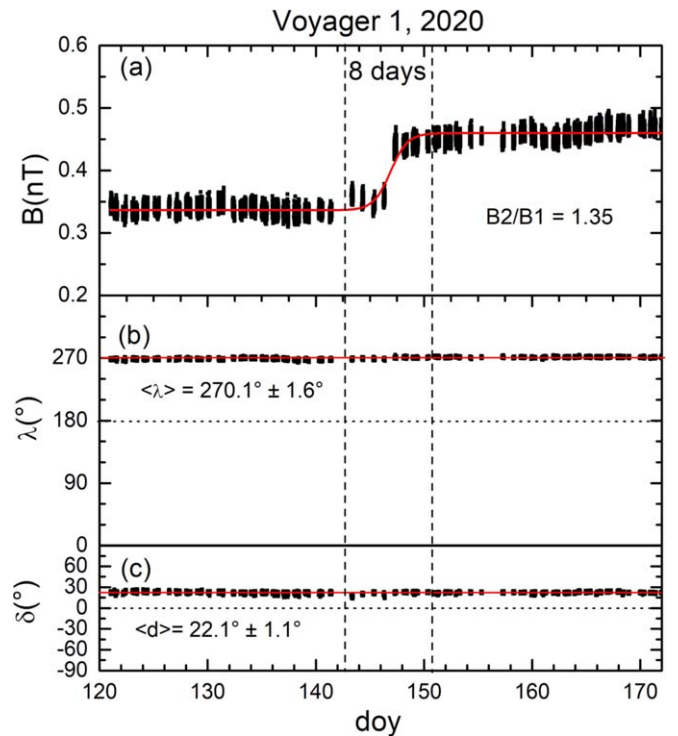


Figure 1. The magnetic field strength (a) azimuthal direction (b), and the elevation angle (c) at a pressure front observed in the VLISM by V1 on 2020/day 147 at 149.27 au. The red curve in panel (a) is a fit to the observations with a sigmoid curve. This event is identified as a pressure front (pf2) that was propagating through the VLISM.

magnetosonic wave, one might also regard it as a “pressure wave front.”

In this paper we support the concept of pressure fronts as presented herein by evidence of jumps in the electron density using spectral averaging of Voyager PWS wideband data that reveal a very weak line at the electron plasma frequency f_{pe} , likely caused by thermal plasma oscillations, i.e., not a beam-driven instability. The spectral averaging is described in the Appendix.

The purpose of this paper is to present recent observations of a fourth major event in the VLISM, the 2020 event, to discuss the nature of this event, and to show that there was a density jump associated with the previous pressure front, pf1, identified by Burlaga et al. (2019). The 2020 event, together with the previous three major events provide a relatively simple view of the structure in the VLISM as we shall show below.

2. The 2020 Event

2.1. The Magnetic Field Observations of the 2020 Event

The most recent major event observed in the magnetic field in the VLISM observed by V1, occurred near day 2020/DOY 147. The event is shown in a plot of the 48 s averages of the magnetic field strength and direction from day 122 to day 172 in Figure 1(a). The observations of $B(t)$ during this interval can be described by the sigmoid function $B(t) = B_2 + [B_1 - B_2] \times [1 + \exp(t - t_0)]$, plotted as the red curve in Figure 1(a), that was obtained by fitting the observations of $B(t)$ with this function. The time of this jump in B can be taken as the time of the inflection point, which occurred on day 2020/146.90.

The passage time of the jump was ~ 8 days, obtained by visual inspection of the data and the curve, which is accurate to

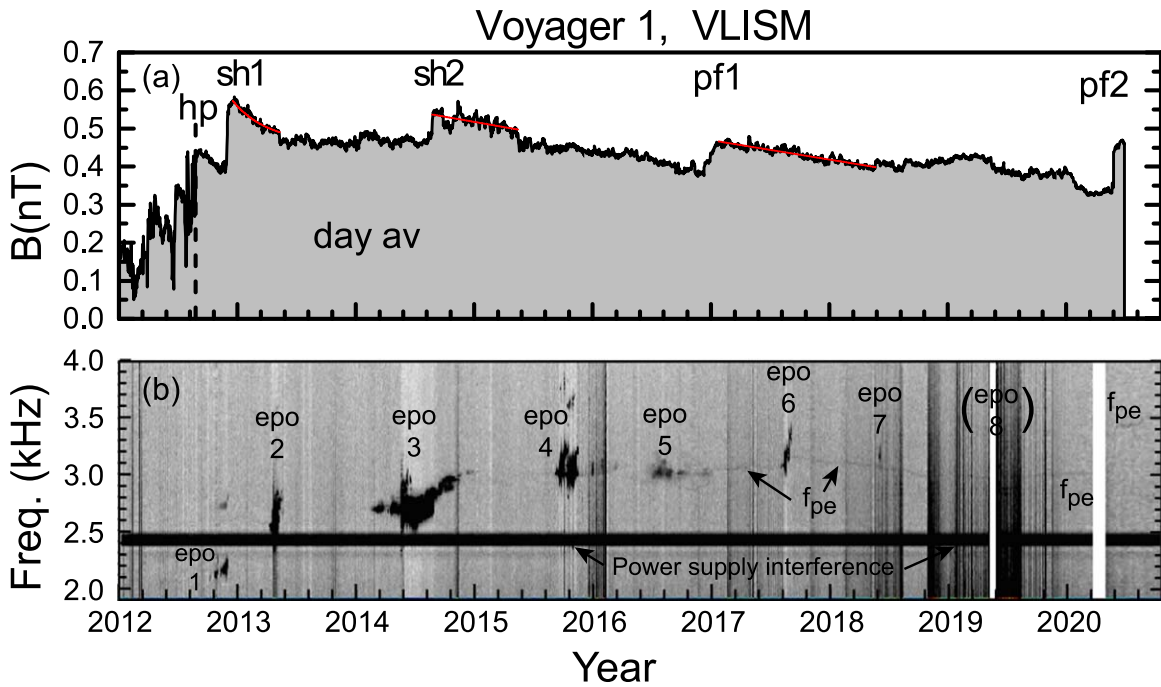


Figure 2. (a) Daily averages of $|B|$ as a function of time. (b) The amplitude of plasma waves between 1.9 and 4.0 kHz as a function of time. The spectrogram is constructed from wideband waveforms acquired as described in the Appendix. Identified with “epo n ” are eight occurrences of intense electron plasma oscillation events described in Gurnett & Kurth (2019) and references therein. These are due to a beam-plasma instability and are associated, in some cases, with the electron foreshocks of shocks related to solar transients that now propagate through the VLISM. The strong line at 2.4 kHz is interference from the spacecraft power supply. The broadband intensifications, particularly from late 2018 to mid-2019 are caused by numerous telemetry errors due to very small signal-to-noise on the Voyager link to the DSN. Of most interest in this panel is a very weak line beginning in 2015 and labeled f_{pe} . This is thought to be a thermal plasma oscillation at the local electron plasma frequency. Note that in 2020 the frequency of this line increases from near 3.0 kHz to about 3.5 kHz. The transition appears to occur at the time of pressure front 2 (pf2) noted in panel (a).

within approximately ± 1 day, considering the data gaps and the uncertainties in the 48 s averages of the data. There was no significant change in the direction of the magnetic field across the increase in B . The average azimuthal angle was $\lambda = 270^\circ \pm 1^\circ \pm 6'$, and the average elevation angle was $\delta = 22^\circ \pm 1^\circ \pm 1'$.

Across the jump in B , the magnetic field strength increased by a factor of 1.35 from 0.34 nT to $B = 0.46$ nT, during an interval of ~ 8 days. The uncertainty in the BT and BN components is approximately 0.02 nT, and the uncertainty in the BR component is larger ~ 0.06 nT, but the BR component itself is very small (see Berdichevsky 2009). Thus, the uncertainty in B is nominally ± 0.035 nT, but the uncertainty in an increment of B during a short interval is less than this because drifts of the magnetometers are generally not important on small scales.

2.2. Density Observations of the 2020 Event

A new method of identifying the plasma frequency, hence density, across the jump in the magnetic field strength has been recently developed and is described in the Appendix. The important point is that the method identifies a new “relatively weak” spectral line, the thermal plasma line, which was not observed prior to 2015, but has been observed quasi-continuously since then on Voyager 1. The spectrogram in Figure 2(b) shows the very weak line beginning in 2015 and continuing through the end of the plotted interval in 2020. As discussed in the Appendix, the origin of this line is likely to be related to thermal plasma oscillations. The line appears at the plasma frequency, from which one can derive the density by the equation $N = (f_{pe}/8980)^2$. The averaged spectra in the latter

portion of the spectrogram in Figure 2 were used to determine N .

While the line at f_{pe} is often faint and difficult to pull out of the data, it is clear that there was a jump in its frequency from early 2020 near 3 kHz to late 2020 where it appears closer to 3.5 kHz. This jump spans the time of the pressure front described in the previous section. Unfortunately, a gap in the data, the ~ 7 day time resolution, and poor visibility of the line just before the jump make it difficult to identify precisely when the jump in frequency occurred. But the time of the change in frequency is clearly consistent with the jump in $|B|$ associated with the pressure front. We have plotted density N derived from the plasma line as a function of time in Figure 3. Prior to the jump, the density averages about 0.11 cm^{-3} . Shortly afterwards, the density is $\sim 0.15 \text{ cm}^{-3}$. From the previous paragraph we have the density jump $N_2/N_1 = \sim 0.15 \text{ cm}^{-3} / \sim 0.11 \text{ cm}^{-3} = \sim 1.36$, in agreement with the jump in B by a factor of 1.35. The abrupt increase in B and N is consistent with compression in the radial direction as a result of an abrupt increase in ram-pressure. Thus, Voyager 1 was observing the front of a compressive MHD wave in the magnetic field and plasma that was passing through a medium dominated by transverse waves.

The ratio $B_2/B_1 = 1.35$ for this 2020 event was somewhat smaller than the ratio $B_2/B_1 = 1.43$ observed at the shock “sh1” on 2012/335.1 in Figure 2 (Burlaga & Ness 2016). The ratio $B_2/B_1 = 1.35$ for this 2020 event was greater than the ratio $B_2/B_1 = 1.13$ observed by Burlaga & Ness (2016) at the shock “sh2” in Figure 2 that moved past V1 on 2014/236.0. In this case, the electron density average before and after that shock was 0.0873 cm^{-3} and 0.0968 cm^{-3} , respectively

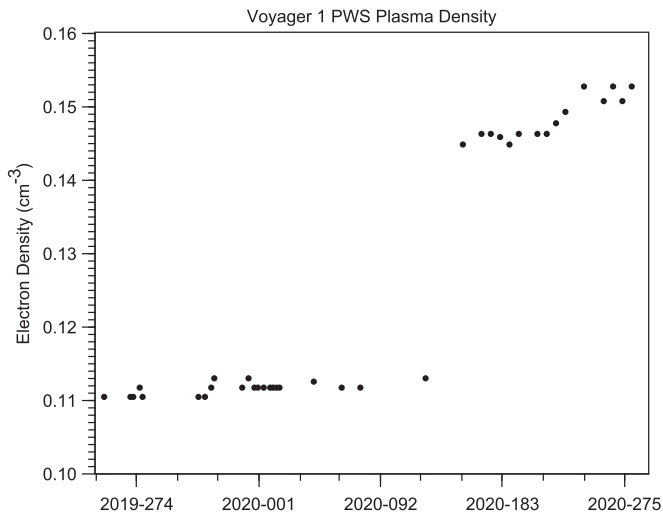


Figure 3. Using spectra like those in Figure 2(b), the frequency of the peak in the weak line at f_{pe} is used to compute the electron number density, which here is plotted vs. time. The low temporal resolution between wideband spectra and periods, when the peak is not present or difficult to discern, results in the low temporal resolution of the density measurement. Nevertheless, a clear jump in the density from near 0.11 to 0.15 cm^{-3} occurs at a time consistent with pf2.

(Gurnett et al. 2015), which gives a density ratio 1.11. Thus, the ratios $B2/B1$ and $N2/N1$ were essentially the same within the uncertainties, consistent with the prediction for a perpendicular shock, $B2/B1 = N2/N1$. Finally, a pressure front pf1 in Figure 2 with $B2/B1 = 1.19$ moved past V1 during 2016/2017 (Burlaga et al. 2019).

2.3. Is the 2020 Event a Pressure Front or a Shock?

We cannot determine whether the 2020 event was a shock or a pressure front on the basis of the size of the jump in B and N alone. The shocks sh1 and sh2 referred to in the introduction and shown in Figure 2(a) were preceded by electron plasma oscillations that ended abruptly when the shock arrived (Gurnett et al. 2013, 2015, respectively). The presence of intense impulsive electron plasma oscillations (of the type normally observed upstream of shocks) strongly supports the interpretation of the jumps in B as shocks. By contrast, the 2020 event, like the pressure front pf1 (Burlaga et al. 2019) was not accompanied by intense impulsive electron plasma oscillations and enhanced energetic particle intensities (S.M. Krimigis 2021, private communication), which suggests that the 2020 event was not a shock with a steepened (i.e., entropy increasing) layer, despite the large compression ratios of its magnetic field and density.

Fraternali et al. (2020) showed that the shock sh2 was associated with strong intermittency in the magnetic field as well as electron plasma oscillations. Thus, such intense, localized intermittency can be a signature of a shock. Figure 4 shows the increments $dB_{48s} = B(t + 48\text{ s}) - B(t)$ for the magnetic field strength B and the components of \mathbf{B} as a function of time. Specifically, the figure shows B in Figure 4(a), the radial component BR of \mathbf{B} in Figure 4(b), the tangential component BT of \mathbf{B} in Figure 4(c), and the normal component of \mathbf{B} in Figure 4(d) as a function of time from day 120 to day 182. If a steepened entropy-increasing shock were present near day 147, indicated by the vertical solid line in each panel, one might expect to see significant changes in the increments of B and the components of \mathbf{B} at that time, as observed by Fraternali

et al. (2020) for sh2. No such change is evident in any of the panels of Figure 4.

The averages of the increments of B and the components of \mathbf{B} before and after the passage of the 2020 event were very close to zero. The standard deviation of the increments, SD , was essentially the same (within the uncertainties) before and after the jump, for the increments of B and each of the components of \mathbf{B} . In particular, the standard deviation of dB was 0.004 nT before the 2020 event and 0.006 nT after it. Similarly, the standard deviation of dB_R , $SD(dB_R)$, was 0.004 nT before the 2020 event and 0.005 nT after it; $SD(BT)$ was 0.005 nT both before and after the 2020 event; and $SD(dB_N)$ was 0.006 nT both before and after it. These values of the standard deviation are essentially all the same, because they correspond to the standard deviations of the Gaussian sensor noise of the magnetometers on Voyager 1.

More importantly, one expects to see an enhancement in the kurtosis K before and after the passage of the 2020 event if it was related to the intermittency produced by a shock, as observed by Fraternali et al. (2020). In the notation used in this paper, the absence of intermittency is given by $K = 0$, and moderate values of intermittency are of the order of $K \sim 5$. Figure 4(a) shows that the intermittency for increments of B was $K = 0.51$ before the 2020 event and $K = 0.49$ after it. Note that these values are similar before and after the 2020 event, and the values are small. The intermittency in the increment of the BR component was $K = 0.02$ before the 2020 event and $K = 0.08$ after, indicating very little intermittency in the signal. The intermittency in the increments of BT was $K = 0.26$ before and $K = 0.32$ after the event; these values are also small and the difference is within the uncertainties. Similarly, the intermittency in the increments of BN was $K = 0.35$ before and $K = 0.20$ after the 2020 event. Again, these values of K are small and their differences are not significant, as can be seen by comparing Figures 4(c) and (d).

Intermittency in the quiet VLISM (excluding shock waves and pressure fronts) was observed by Burlaga et al. (2020). They considered the distribution of 1 hr increments of B and the components of \mathbf{B} , and found that it could be fitted with a q -Gaussian distribution with $q = 1.22 \pm 0.03$. (q -Gaussian distributions were introduced by Tsallis et al. in the context of nonextensive statistical mechanics (Tsallis 1988, 2004a, 2004b). To put this number in perspective, note that $q = 1$ for a Gaussian distribution, and in the heliosheath q can be as high as 1.8. Thus, the “intermittency” (the deviation from a Gaussian distribution measured by q), was small but statistically significant in the VLISM.

Let us consider whether the fluctuations in Figure 4 are entirely Gaussian noise, or whether there was some intermittency in the signal associated with the background magnetic field of the quiet VLISM. Since B depends on all of the components of \mathbf{B} , it is sufficient to compute the distribution of increments of B in order to identify the presence of intermittency in the observations. A plot of the distribution of the increments of 48 s averages of B in the interval from 2020, DOY 120 to 182 is shown in Figure 5. The distribution of these increments of B can be described accurately by q -Gaussian distribution function with the nonextensivity parameter $q = 1.21 \pm 0.03$, which is shown as the solid curve in Figure 5. Thus, the observation of q near the 2020 event is consistent with the observations of intermittency in the quiet

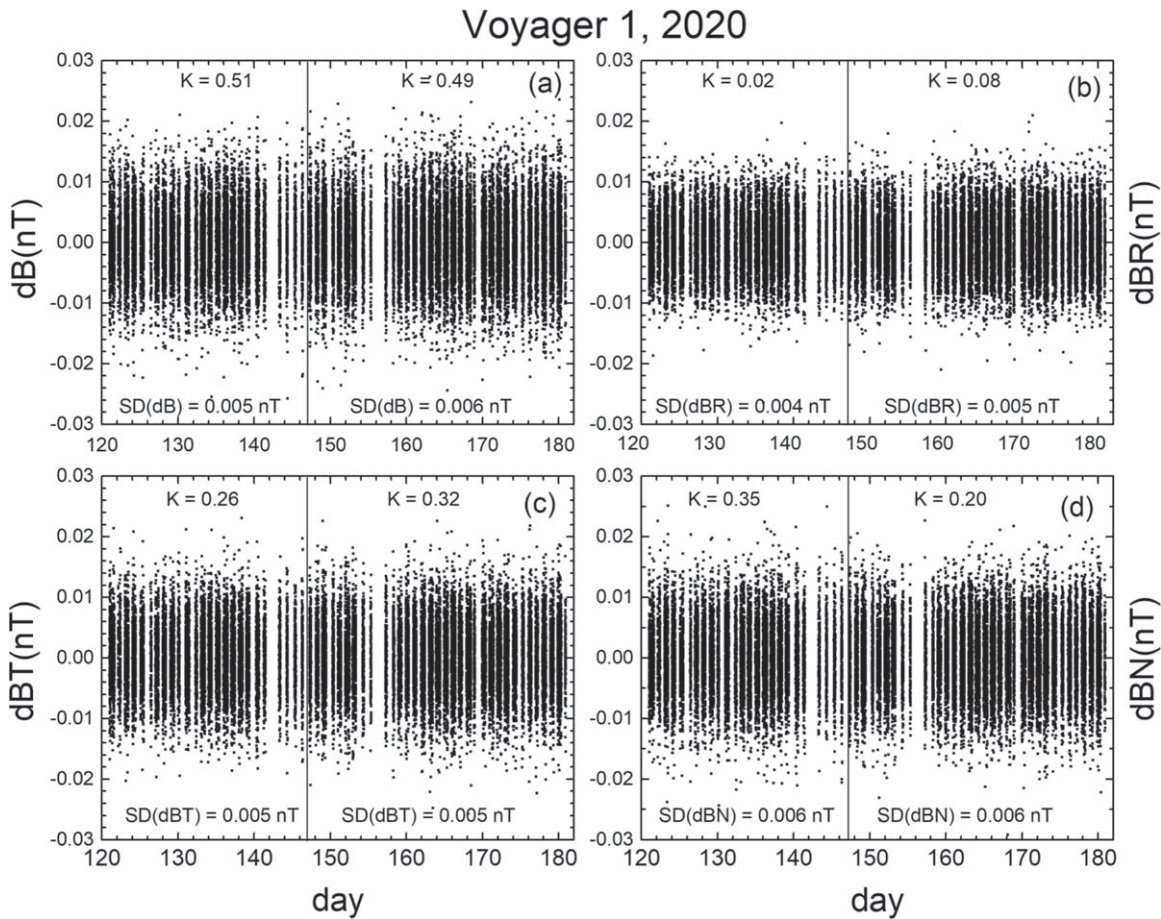


Figure 4. The 48 s averages of 48 s increments of B and the components of B : dB (a), dBR (b), dBT (c), and dBN (d) observed by V1 in the VLISM from day 120 to day 182, 2020.

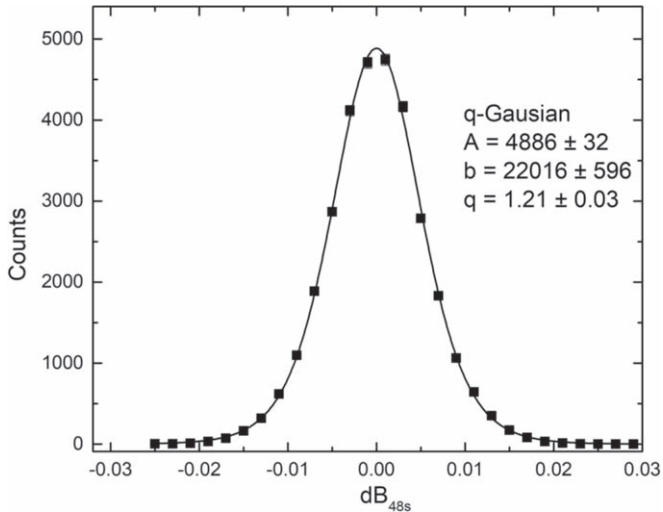


Figure 5. The distribution of the 48 s averages of the 48 s increments of B from day 130 to day 180, 2020. The solid curve is a q -Gaussian fit to the distribution.

VLISM based on 1 hr increments of the magnetic field. There is no evidence for fluctuations in Figure 5 that might have been produced by a shock, which would have produced a significantly larger intermittency (Fraternali et al. 2020). Thus, intermittency was present during the interval between day 130 and day 180, 2020, but it was not produced by a pressure front or shock. Rather, the intermittency was a

property of the background magnetic field in the VLISM, as demonstrated by Burlaga et al. (2020).

In conclusion, there is no evidence for intense spiky upstream electron plasma oscillations, enhanced energetic particle intensities, or relatively strong intermittency associated with the 2020 event that might suggest the presence of a steepened entropy producing shock. Thus, we conclude that the 2020 event is most probably a magnetic field/plasma (MHD) pressure front associated with a compressive wave, that we denote by pf2.

Let us consider the possibility that the observations that led us to identify pressure front pf2 might be interpreted as evidence for two pressure fronts, one overtaking the other. Figure 6 shows a fit to the observations in which the jump in B is regarded as two separate jumps corresponding to the passage of two pressure waves, one overtaking the other. Two sigmoid fits to the observations were used to obtain the red curve shown in Figure 6. The first jump in B was $B_2/B_1 = 1.04$. The second jump corresponds to $B_3/B_2 = 1.28$ giving a total jump $B_2/B_1 = 1.33$, which is comparable to $B_2/B_1 = 1.43$ in shock sh1 (Burlaga & Ness 2016). Thus, one can fit the observations with two jumps in B , with the introduction of three additional parameters. However, the probability that one would observe such a configuration is very small. Thus, we can conclude that the observations are most likely evidence of the passage of a single pressure front, pf2.

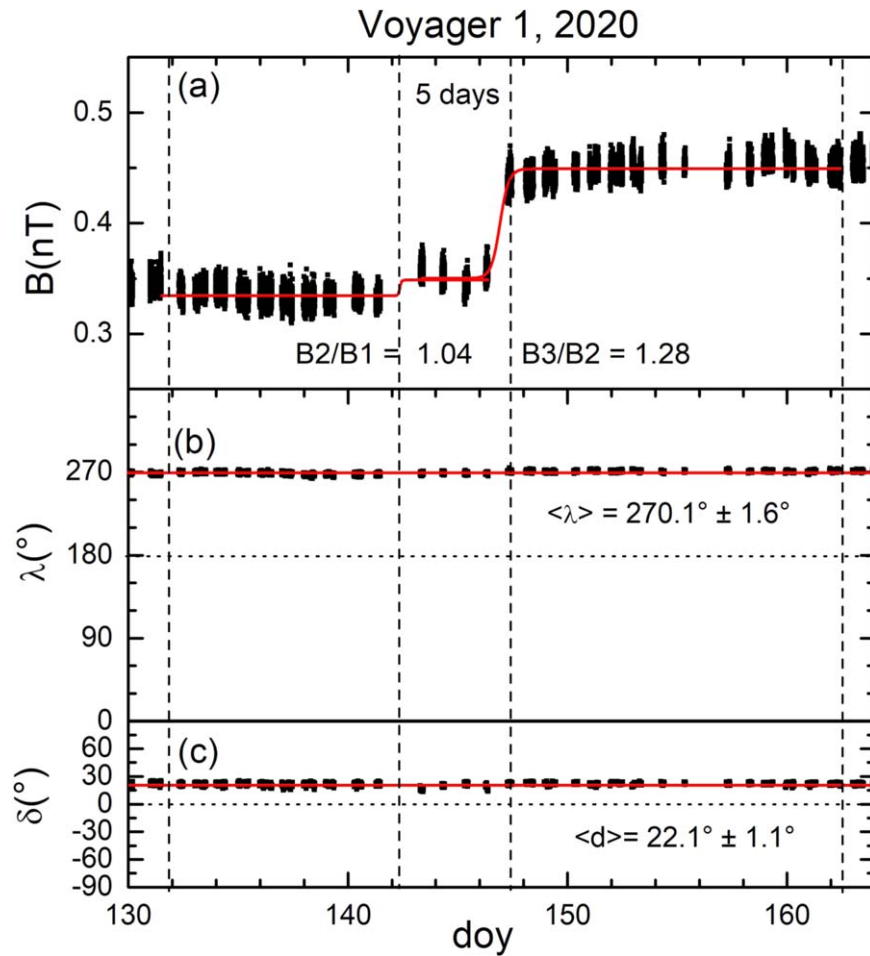


Figure 6. A plot of B from day 130 to day 164 of the 48 s averages of B (a), the azimuthal angle (λ), and the elevation angle (δ). This figure shows that one can fit the observations of B in Figure 3 with two sigmoid curves. One could interpret the observations as overtaking one pressure front by another, within the uncertainties of the observations, but the probability of observing such an event is very small. The simplest and most probable fit to the observations is that in Figure 1.

2.4. Why Was the Jump in B Larger in pf2 than pf1?

The magnetic field strength increased by a factor of 1.33 in pf2, compared to a factor of 1.19 for pf1. Thus, even though pf2 was farther from the Sun than pf1, the increase in B at pf2 was larger than that at pf1. In fact, the jump in B at pf2 was nearly as large as that for the jump at the shock sh1, namely 1.43. How does one explain the relatively large size of the jump at pf2? We also observed that pf2 moved past V1 in ~ 8 days, compared to 35 days for the pressure front pf1 observed during 2017, which also must be explained. One possibility is simply that a series of merged interaction regions in the heliosheath coalesced to produce a very strong pressure pulse at the heliopause, which then evolved to the size of the jump at pf2. Another possibility is that larger size of the jump at pf2 was the result of the steepening of the pressure front with increasing time and distance, possibly augmented by the overtaking of one pressure pulse by another within the VLISM to produce the single pressure pulse pf2. The validity of these hypotheses should be investigated by theorists.

2.5. Pressure Front pf1

We return to pf1 armed with the ability to use the PWS data to look for a corresponding increase in density. We show in Figure 7(a) a wideband spectrogram from 2016/035 to 2017/239 covering the frequency range from 1.9 to 4.0 kHz. The two

most prominent features in this spectrogram are two electron plasma oscillation events (labeled epo 5 and epo 6) that correspond to features similarly identified in Figure 2. However, the feature of interest in the top spectrogram (Figure 7(a)) is a very weak line labeled f_{pe} . This line is near 3 kHz, throughout. However, after epo 5, there is a time period with two lines, one somewhat broader and stronger at 3.0 kHz and another that is very fine and weak, closer to 2.9 kHz. We interpret the emission at 3.0 kHz as a radio emission, probably generated at the epo 5 before day 245. The lower frequency line is interpreted as a weak thermal plasma emission at f_{pe} . Hence, the radio emission is propagating into a somewhat lower density region until it ends at the beginning of 2017. Figure 7(b) shows the same spectrogram but with the fine line at f_{pe} digitized at various times highlighted by a black line. Near the beginning of 2017 the frequency increases to about 3.0 kHz, which is likely the reason the radio emission ends, as it cannot propagate at frequencies at or below f_{pe} . In Figure 8 we have plotted the electron density N given by $(f_{pe}/8980)^2$, where f_{pe} is in Hz and N is in cm^{-3} . The jump in density is from about 0.104 to about 0.116 cm^{-3} for a ratio of $N_2/N_1 \sim 1.12$. Hence the jump in N for pressure front is reasonably close to the jump in B .

Voyager 1 PWS Wideband Data

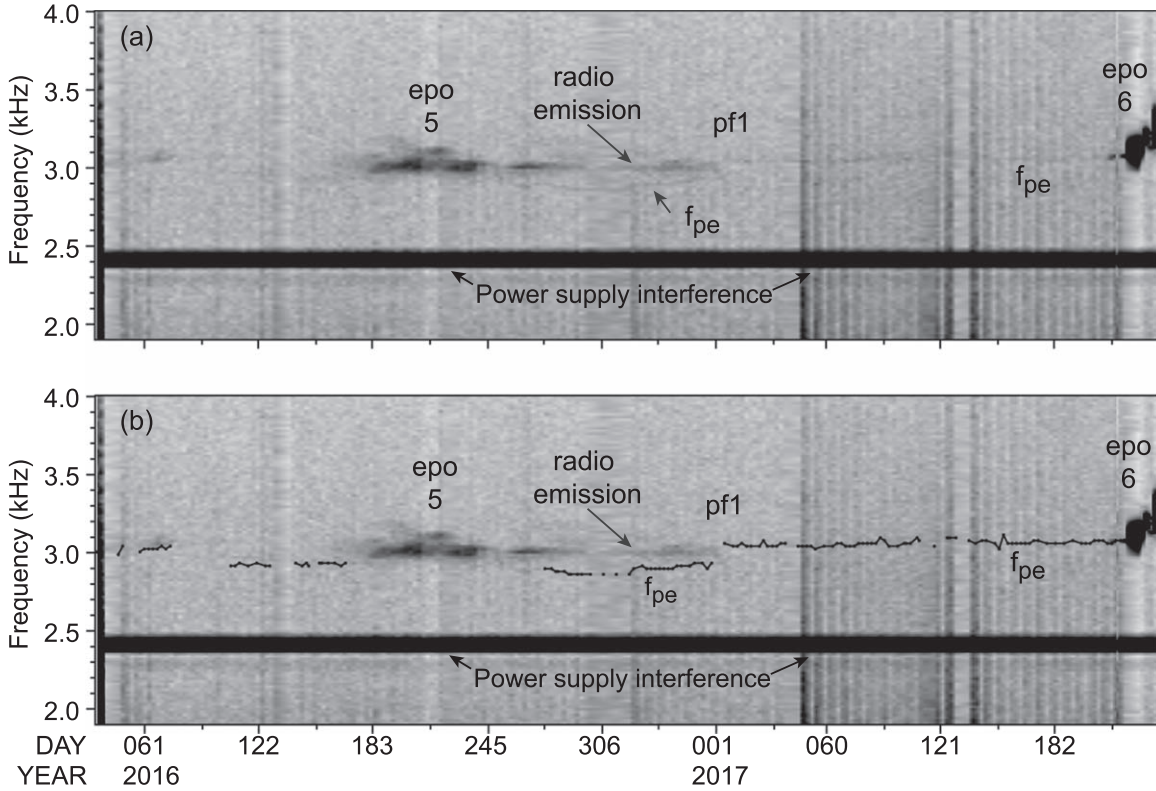


Figure 7. (a) Spectrogram showing a faint line at f_{pe} that increases in frequency near the beginning of 2017, about the time of the pressure front pf1 discussed in the text. (b) The spectrogram is the same as the top, but the line at the plasma frequency is highlighted with a black line.

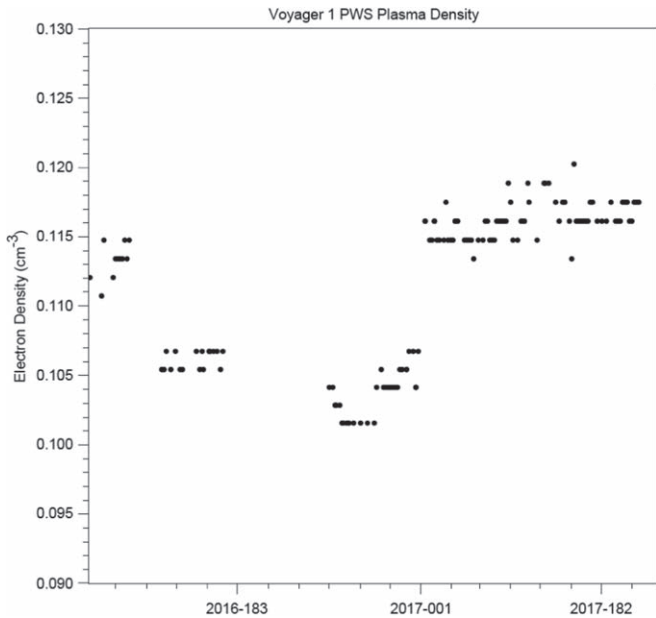


Figure 8. Electron densities derived from the line at the plasma frequency in Figure 2. A clear increase is seen at the end of 2016.

3. Summary and Discussion

We have confirmed the existence of pressure fronts in the VLISM by identifying a second pressure front, observed by V1 on 2020/147, at 149 au, $34^{\circ}8$ latitude, and $175^{\circ}3$ longitude in heliographic inertial coordinates. We have used a new technique to show that each of these jumps in the field was accompanied by a similar increase in the plasma density. The

increase in B at this pressure front, $B_2/B_1 = 1.33$, was significantly greater than that observed in the previous pressure front pf1 ($B_2/B_1 = 1.19$ on 2016.9/237), and in the previous shock sh2 ($B_2/B_1 = 1.13$ on 2014.6/346). The largest increase in B observed by V1 in the VLISM was associated with the shock sh1 ($B_2/B_1 = 1.43$, on 2012.9746/DOY 335).

We conclude this paper with a brief discussion of the role of shocks and pressure fronts in the overall structure of the VLISM observed by V1, from the time of the heliopause crossing in 2012/238 to the most recent observations on day 182, 2020, in the context of all of the magnetic field observations to date in the VLISM. These observations are shown in Figure 2(a). There are two striking results in Figure 2: (1) there were just four prominent maxima of B in the VLISM during the 8 yr interval; (2) the maxima of B were causally related to the two shocks (sh1 and sh2) and the two pressure fronts (pf1 and the new event pf2) discussed above.

Each of these maxima in B was associated with a relatively rapid increase in B (the jump in B) to a maximum value, followed by a relatively slow decrease in B (a ramp). Thus, each of the features associated with a maximum in B had a jump-ramp structure and two associated timescales. These jump-ramp structures were separated by larger quiet regions in which B varied relatively slowly, and contained small amplitude waves and turbulence. Thus, the basic structure of the VLISM observed between 2012/DOY 238 and 2020/DOY 182 consists of four jump-ramp structures associated with the four maxima in B between 2012 and 2020, separated by four quiet intervals.

The timescales of the jumps that moved past V1 were ~ 5.4 days and 3.3 days for the shocks sh1 and sh2 observed on

~ 2012.9746 (DOY 335) and 2014.6 (DOY 236), respectively. The corresponding timescales for the jumps associated with pressure fronts were ~ 35 days and ~ 8 days for the pressure fronts pf1 and pf2 observed on $\sim 2016/346$ and $\sim 2020/147$, respectively. The corresponding timescale for the ramp associated with sh1 was ~ 162 days, during which time B decreased exponentially from $\sim 2012.9746/335$ to $\sim 2013.35759/131$. The timescale of the ramp associated with sh2 was 276 days, when B decreased linearly (with notable fluctuations related to fine-scale features) from 2014.68212 to 2015.37669. In the ramp following the pressure front pf1, B declined nearly monotonically until 2018.41885, during an interval of 402 days. We do not yet have V1 observations during the ramp associated with pf2.

We have shown that jump–ramp features of B in the VLISM and the larger quiet intervals between them are the fundamental features of the VLISM. These features were actually specially configured waves that were generated by the interaction of heliosheath with the heliopause and then propagated through the VLISM, presumably interacting with one another to produce the results observed by Voyager 1. Smaller scale waves and turbulence exist within these features. Mathematical techniques such as Hilbert transforms and wavelet transforms (Zhao et al. 2020) and Fourier methods (Fraternali et al. 2019) are very valuable tools for studying the VLISM over a wide range of scales. However, it is also essential to understand the basic structure and dynamics of the large-scale flows on scales of hours to a decade presented in this paper. This can best be done by improving the MHD models and the corresponding input observations. A number of models have been discussed in the literature, including those by Fermo et al. (2015), Zirnstein et al. (2018), and Kim et al. (2017). However, none of these models reproduce the kind of pattern of shocks, pressure pulses, and quiet regions shown in Figure 2.

Appendix New Method for Deriving Plasma Densities

The Voyager PWS instrument (Scarf & Gurnett 1977) includes a wideband waveform receiver that captures digitized waveforms in the range of 50 Hz to above 10 kHz. Waveform captures include 1600 4 bit samples obtained at a rate of 28,800 samples per second. On board, 800 of these waveform captures are obtained at a rate of one every 60 ms covering 48 seconds (one frame). Due to decreasing telemetry performance at the large distances of Voyager, beginning in 1992 November, only one of every five waveform captures has been transmitted to the ground. Hence, 55.56 ms of waveforms are returned for every 300 ms, for a duty cycle of 18.5%. The 1600 waveform samples provide a spectral resolution of about 18 Hz if a 1600 point Fourier transform is used. It should be mentioned that an automatic gain controlled (AGC) amplifier is included in the wideband receiver to ensure the received waveform makes optimal use of the 4 bit digitization space. Unfortunately, the gain of the AGC could not be telemetered to the ground, so only relative amplitudes can be determined from these data.

For the last several years, up to three of these wideband waveform frames have been recorded on the digital tape recorder and transmitted to the ground every few months. In 2020, the nominal rate of recording frames has been reduced to 1 frame per week. In reality, since it now requires an array of four Deep Space Stations (DSS) (one 70 m and three 34 m antennas) at one of the Deep Space Network (DSN) complexes

to achieve a usable signal-to-noise ratio to successfully transmit the wideband data, the ability to schedule the DSN for the playback is difficult and does not always occur before older data is overwritten on board. This can cause gaps in the observations. Further, even with a four-station array, the signal-to-noise ratio is very low, and telemetry errors are frequent, especially if the weather is poor at the DSN complex. These telemetry errors occur as a random change in one or more of the four bits in a measurement, resulting in spikes in the received waveform that are unrelated to the recorded waveform.



In order to bring out weak features in the wideband spectrum, the waveforms are first cleaned using a despiking algorithm that looks for telemetry error-induced spikes and attempts to replace these with more reasonable values. Given that the spectral features such as plasma oscillations typically do not change in frequency on the timescale of 48 s, spectra from all available waveform captures in a frame can be averaged to improve the noise level of the resulting spectrum. Finally, by constructing a long-time interval spectrogram in which each averaged spectrum is arranged side-by-side according to the time of the frames, even longer spectral averages can be achieved. If the spectral features do not change frequency, significantly, this additional spectrum averaging can improve the noise level, further. S. Ocker et al. (2021, in preparation) have independently applied a number of techniques to increase the signal-to-noise ratio in the Voyager wideband data.

Figure 2(b) is the result of the spectral averaging methods described above. The bright features labeled “epo n ” late in 2012 ($n = 1$), early 2013 (2), mid-2014 (3), late 2015 (4), mid-2016 (5), mid-2017 (6), and briefly in mid-2018 (7) are electron plasma oscillation events resulting from a beam-plasma instability discussed in several papers (Gurnett et al. 2013, 2015, 2021; Gurnett & Kurth 2019). An event in 2019 (epo 8) is not visible in this spectrogram due to the combined effects of telemetry errors in the wideband data and spectral averaging.

What is new and very important in this spectrogram, however, is a very faint line beginning in 2015 that more-or-less connects the electron plasma oscillations. The origin of this line is not well understood at this time, but is likely a thermal plasma oscillation at the electron plasma frequency, or perhaps the peak of the quasi-thermal noise (QTN) spectrum (see, for example, Meyer-Vernet & Perche 1989; Le Chat et al. 2009). This latter possibility is deemed problematic because the 10 m antenna utilized by the PWS instrument is short compared to the Debye length (tens of meters) in the interstellar plasma, hence the predicted peak in the QTN spectrum at f_{pe} is essentially negligible in the QTN theory. Regardless of the origin of this faint line, the fact that it varies in frequency makes it unlikely to be an interference line, especially since interference in this frequency range has not previously been identified. That the line connects to previously observed intense shock-driven upstream plasma oscillation events argues that the line is almost certainly at the electron plasma frequency f_{pe} .

ORCID iDs

L. F. Burlaga  <https://orcid.org/0000-0002-5569-1553>
 W. S. Kurth  <https://orcid.org/0000-0002-5471-6202>
 D. A. Gurnett  <https://orcid.org/0000-0003-2403-0282>
 L. K. Jian  <https://orcid.org/0000-0002-6849-5527>

J. Park  <https://orcid.org/0000-0002-8989-4631>
 A. Szabo  <https://orcid.org/0000-0003-3255-9071>

References

- Behannon, K. W., Acuña, M. H., Burlaga, L. F., et al. 1977, *SSRv*, **21**, 235
 Berdichevsky, D. B. 2009, White Paper, Voyager Mission, Detailed Processing of Weak Magnetic Fields I—Constraints to the Uncertainties of the Calibrated Magnetic Field Signal in the Voyager Missions, https://vgrmag.gsfc.nasa.gov/Berdichevsky-VOY_sensor_opu090518.pdf
 Burlaga, L. F., Berdichevsky, D. B., Jian, L. K., et al. 2021, *ApJL*, **906**, 119
 Burlaga, L. F., & Ness, N. F. 2016, *ApJ*, **829**, 1341
 Burlaga, L. F., Ness, N. F., Berdichevsky, D. B., et al. 2019, *ApJ*, **877**, 31
 Burlaga, L. F., Ness, N. F., Berdichevsky, D. B., et al. 2020, *ApJL*, **901**, L2
 Burlaga, L. F., Ness, N. F., Gurnett, D. A., & Kurth, W. S. 2013a, *ApJL*, **778**, L3
 Burlaga, L. F., Ness, N. F., & Richardson, J. D. 2014, *JGR*, **119**, 6062
 Burlaga, L. F., Ness, N. F., & Stone, E. C. 2013b, *Sci*, **341**, 147
 Burlaga, L. F., Ness, N. F., Richardson, J. D., Decker, R. B., & Krimigis, S. M. 2016, *ApJ*, **818**, 147
 Fermo, R. L., Pogorelov, N. V., & Burlaga, L. F. 2015, *JPhCS*, **642**, 012008
 Fisk, L. A., & Gloeckler, G. 2014, *ApJ*, **789**, 41
 Fraternali, F., Pogorelov, N., & Burlaga, L. F. 2020, *ApJL*, **897**, L28
 Fraternali, F., Pogorelov, N. V., Richardson, J. D., & Tordella, D. 2019, *ApJ*, **872**, 40
 Gloeckler, G., & Fisk, L. 2016, *ApJ*, **833**, 290
 Gloeckler, G., & Fisk, L. A. 2014, *GeoRL*, **41**, 5325
 Gurnett, D. A., & Kurth, W. S. 2019, *NatAs*, **3**, 1024
 Gurnett, D. A., Kurth, W. S., Allendorf, S. C., & Poynter, R. L. 1993, *Sci*, **262**, 199
 Gurnett, D. A., Kurth, W. S., Burlaga, L. F., & Ness, N. F. 2013, *Sci*, **341**, 1489
 Gurnett, D. A., Kurth, W. S., Stone, E. C., et al. 2015, *ApJ*, **809**, 121
 Gurnett, D. A., Kurth, W. S., Stone, E. C., et al. 2021, *AJ*, **161**, 11
 Holzer, T. E. 1989, *ARA&A*, **27**, 99
 Karmesin, S. R., Liewer, P. C., & Brackbill, J. U. 1995, *JGR*, **78**, 53
 Kim, T. K., Pogorelov, N. V., & Burlaga, L. F. 2017, *ApJL*, **843**, 32
 Krimigis, S. M., Decker, R. B., Roelof, E. C., et al. 2013, *Sci*, **341**, 144
 Le Chat, G., Issautier, K., Meyer-Vernet, N., et al. 2009, *PoP*, **16**, 102903
 McComas, D. J., Angold, N., Elliott, H. A., et al. 2013, *ApJ*, **779**, 2
 McComas, D. J., Bzowski, M., Frisch, P., et al. 2010, *JGRA*, **115**, A09113
 Meyer-Vernet, N., & Perche, C. 1989, *JGR*, **94**, 2405
 Mostafavi, P., & Zank, G. P. 2018a, *ApJL*, **854**, L15
 Mostafavi, P., & Zank, G. P. 2018b, *JPhCS*, **1100**, 012018
 Parker, E. N. 1958, *ApJ*, **128**, 664
 Parker, E. N. 1961, *ApJ*, **134**, 20
 Pogorelov, N. V., Fichtner, H., Czechowski, A., et al. 2017, *SSRv*, **212**, 193
 Richardson, J. D., Wang, C., Liu, Y. D., et al. 2017, *ApJ*, **834**, 190
 Scarf, F. L., & Gurnett, D. A. 1977, *SSRv*, **21**, 289
 Stone, E. C., Cummings, A. C., McDonald, F. B., et al. 2013, *Sci*, **341**, 150
 Tsallis, C. 1988, *JSP*, **52**, 479
 Tsallis, C. 2004b, *PhyA*, **340**, 1
 Tsallis, C. 2004b, in *Nonextensive Entropy: Interdisciplinary Applications*, ed. M. Gell-Mann & C. Tsallis (New York: Oxford Univ. Press), 1
 Wang, C., & Belcher, J. W. 1999, *JGR*, **104**, 549
 Washimi, H., Tanaka, T., & Zank, G. P. 2017, *ApJL*, **846**, L9
 Washimi, H., Zank, G. P., Hu, Q., et al. 2011, *MNRAS*, **416**, 1475
 Whang, Y. C., & Burlaga, L. F. 1995, *JGR*, **100**, 17023
 Zank, G. 2015, *ARA&A*, **53**, 449
 Zank, G. P. 1999, *SSRv*, **89**, 413
 Zank, G. P., & Müller, H.-R. 2003, *JGRA*, **108**, 1240
 Zhao, L.-L., Zank, G. P., & Burlaga, L. F. 2020, *ApJ*, **900**, 166
 Zirnstein, E. J., Heerikhuisen, J., McComas, D. J., et al. 2018, *ApJ*, **859**, 104